Synthesis of mesoporous ZIF-8 nanoribbons and their conversion into carbon nanoribbons for high-performance supercapacitors

CHEMISTRY
A European Journal

A Journal of
ChemPubSoc Europe

Accepted Article

Title: Synthesis of Mesoporous ZIF-8 Nanoribbons and Their Conversion into Carbon Nanoribbons for High-Performance Supercapacitors

Authors: Feng Wang, Xueqing Yang, Wei Chen, Haidong Bian, Tianying Sun, Yangyang Du, Zhenyu Zhang, Wenjun Zhang, Yangyang Li, and Xianfeng Chen

To be cited as: *Chem. Eur. J.* 10.1002/chem.201801869

Link to VoR: http://dx.doi.org/10.1002/chem.201801869

Supported by
ACES

WILEY-VCH

10.1002/chem.201801869

WILEY-VCH

Synthesis of Mesoporous ZIF-8 Nanoribbons and Their Conversion into Carbon Nanoribbons for High-Performance Supercapacitors

Xueqing Yang,[a,d] Wei Chen,[a,d] Haidong Bian,[a] Tianying Sun,[a,d] Yangyang Du,[a,d] Zhenyu Zhang,[a] Wenjun Zhang,[a,b] Yangyang Li,[a] Xianfeng Chen,[c] Feng Wang*[a,d]

Abstract: ZIF-8 nanoribbons with tunable morphology and pore structure were synthesized by using tri-block co-polymer Pluronic F127 as a soft template. The as-synthesized ZIF-8 nanoribbons were converted into carbon nanoribbons by thermal transformation with largely preserved morphology and porosity. The resulting carbon nanoribbons feature both micro- and meso-pores with high surface areas of over 1000 $m^2 g^{-1}$. In addition, nitrogen-doping in the carbon nanoribbons was achieved as was confirmed by XPS and EELS measurements. The hybrid carbon nanoribbons provide pseudo-capacitance that promotes electrochemical performance, rendering a high specific capacitance of up to 297 F g^{-1} at a current density of 0.5 A g^{-1} in a three-electrode system. A long cycle life was also demonstrated by recording a 90.26% preservation of capacitance after 10, 000 cycles of charge-discharge at a current density of 4.0 A g^{-1}. Furthermore, a symmetrical supercapacitor is fabricated by employing the carbon nanoribbons, which shows good electrochemical performance with respect to energy, power and cycle life.

Introduction

One-dimensional porous carbon nanomaterials are promising for applications in energy storage, water treatment, and biomedicine due to their excellent chemical and physical properties, such as high specific surface area, high chemical stability[1, 2]. One-dimensional nanoribbons are advantageous over zero-dimensional nanoparticles as building blocks for energy applications. This is because continuous contact between nanoribbons can be easily established, leading to a low percolation threshold.[3] Over the past decades, various methods including arc discharge, laser ablation, and chemical vapour deposition have been developed to synthesize porous carbon nanomaterials[4, 5]. A common strategy is the hard-template method that uses solid sacrificing templates (e.g.; silica[6], zinc oxide[7], and zeolites[8]) to control the formation of target nanomaterials. Despite the great success in preparing a variety of porous carbon materials, this method is typically accompanied by tedious and complex steps for removal of template materials[1]. Furthermore, challenge remains for efficient and scalable syntheses of carbon nanoribbons with concurrent control over the pore structures that are critical for practical applications. Thus, it is of high significance to develop an efficient and straightforward method for preparing carbon nanoribbons with rational control over porosity.

In recent years, thermal transformation of metal-organic frameworks (MOFs) has emerged as a promising strategy for preparing porous nanomaterials[9-12]. MOFs are porous crystalline materials with metal-ligand backbones connected by coordination bonds[13-15]. By pyrolysis under precisely controlled conditions, MOF materials can transform into various carbon derivatives with largely preserved morphology and pore structure. Owing to the high designability and tunability of precursor MOFs, the derived carbon materials can be endowed with unprecedented functionalities[16-19]. For example, controlling the growth of parent MOFs has enabled novel carbon nanoribbons and graphene nanoribbons that were shown to be promising electrode materials in supercapacitors[19]. Porous carbon nanomaterials such as hollow carbon nanocubes and hierarchical carbon nanofibers have also been fabricated by thermal transformation of ZIF-8, a sodalite (SOD)-type MOF consisted of a zinc ion centre and 2-methylimidazole (Hmim) ligand[20-27]. ZIF-8 is advantageous as precursor crystals due to the zeolite-like structure that provides high porosity as well as high chemical and thermal stability under ambient environment. Furthermore, nitrogen atoms in the aromatic ring of methylimidazole ligand can be readily preserved and incorporated into the matrix of resultant carbon materials[28-32].

In this paper, we present an approach for engineering the morphology and pore structure of MOF-derived carbon nanomaterials by controlling the formation of ZIF-8 precursor crystals with tri-block co-polymer Pluronic F127. We show that F127 directs the formation of one-dimensional morphology in addition to creating extra pores in ZIF-8 nanocrystals, which leads to the formation of novel nanoribbon-shaped carbon nanomaterials with a bimodal distribution of pores through pyrolysis. This unique microstructure is able to produce high-performance supercapacitors.

Results and Discussion

The synthetic procedure of porous carbon nanoribbons is illustrated in Scheme 1. ZIF-8 nanoribbons were first synthesized in an aqueous solution by incubating zinc nitrate hexahydrate and F127 prior to reaction with Hmim. ZIF-8

[a] Department of Materials Science and Engineering, City University of Hong Kong, 83 Tat Chee Avenue, Hong Kong SAR, China. E-mail: fwang24@cityu.edu.hk

[b] Center of Super-Diamond and Advanced Films (COSDAF), City University of Hong Kong, 83 Tat Chee Avenue, Hong Kong SAR, China.

[c] Institute for Bioengineering, School of Engineering, University of Edinburgh, Edinburgh, United Kingdom

[d] City University of Hong Kong Shenzhen Research Institute, Shenzhen 518057, China

Supporting information for this article is given via a link at the end of the document.

nanoribbons were then calcinated at 1000 °C to form carbon nanoribbons, followed by activation with KOH at 800 °C.

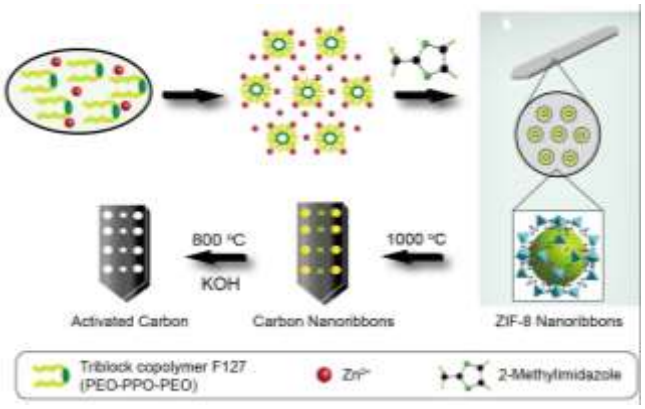

Scheme 1. Schematics of F127-assisted synthesis of ZIF-8 nanoribbons and their thermal transformation into porous carbon nanoribbons.

In an aqueous synthesis of ZIF-8 crystals, the ratio of Zn ion to Hmim plays a major role[33]. In our experiments, a high ratio of Hmim to Zn ion was used to promote crystal growth and to minimize formation of byproducts such as $Zn(OH)_2$, $Zn(OH)(NO_3)$ (H_2O), and $Zn_5(OH)_8(NO_3)_2(H_2O)_2$[34]. F127 was introduced to control the growth of ZIF-8 crystals by mediating an evaporation induced self-assembly process[35]. F127 with the formula $(PEO)_{106}(PPO)_{70}(PEO)_{106}$ is a block polymer comprising both hydrophobic (PPO) and hydrophilic (PEO) segments. In an aqueous solution, F127 tends to self-assemble and form micelles with hydrophobic PPO cores surrounded by hydrophilic PEO coronas[35, 36]. The formed micelles attract Zn ions to their surface and initiate nucleation of ZIF-8 crystals on addition of Hmim ligands. When the solvent was gradually evaporated in subsequent reactions, primary particles formed around individual F127 micelles started to assemble and coalesce, leading to the growth of ZIF-8 nanoribbons. The scanning electron microscopy (SEM) images of intermediate products obtained at different reaction times clearly show the formation of small particles and the coalescence of primary particles (Figure S1), supporting the evaporation induced self-assembly process[36].

As shown in Figure 1a, the nanocrystals prepared in the absence of F127 display a polyhedral morphology, which is in good agreement with previous reports[37, 38]. With the addition of F127, thin ribbon-like nanocrystals appear and the size of the nanoribbons is tuned from 0.21 × 0.91 μm to 0.49 × 2.30 μm by increasing the F127 concentration from 0.125 to 0.500 wt% (Figure 1b-e). At low F127 concentrations, the number of PEO segments is too small to accommodate all the nuclei, thereby leading to the formation of a binary mixture of nanoparticles and nanoribbons (Figure 1b). With increasing F127 concentrations, the cross-linking between primary nanoparticles is enhanced, resulting in the formation of large nanoribbons (Figure 1c-e). In comparison, only small-sized ZIF-8 nanoparticles were obtained at a substantially high concentration of F127 (i.e.; 1.000 wt%) (Figure 1f). The results are due to a fast nucleation enabled by a large amount of F127, which results in a reduced rate of crystal growth and coalescence in subsequent reactions.

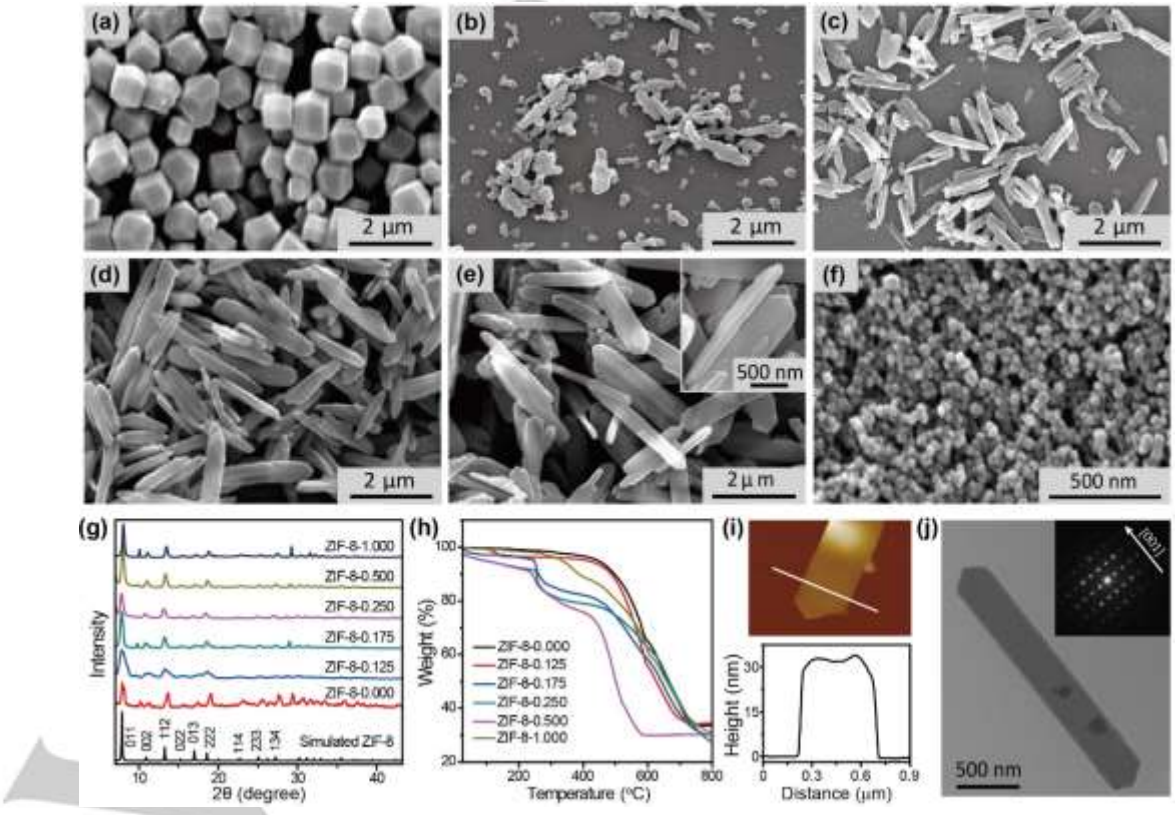

Figure 1. (a-f) SEM images of ZIF-8 crystals synthesized at F127 concentrations of 0.000 wt% (ZIF-8-0.000), 0.125 wt% (ZIF-8-0.125), 0.175 wt% (ZIF-8-0.175), 0.250 wt% (ZIF-8-0.250), 0.500 wt% (ZIF-8-0.500), and 1.000 wt% (ZIF-8-1.000), respectively. Inset (e): magnified SEM image of a ZIF-8 crystal revealing the ribbon-like morphology. (g) XRD patterns and (h) TGA curves of the as-synthesized ZIF-8 nanoribbons as a function of F127 concentration in the synthesis. (i) AFM image and corresponding height profile of typical ZIF-8 nanoribbon synthesized in the presence of 0.500 wt% F127. (j) TEM image of a ZIF-8-0.500 nanoribbon. Inset: electron diffraction pattern of the nanoribbon.

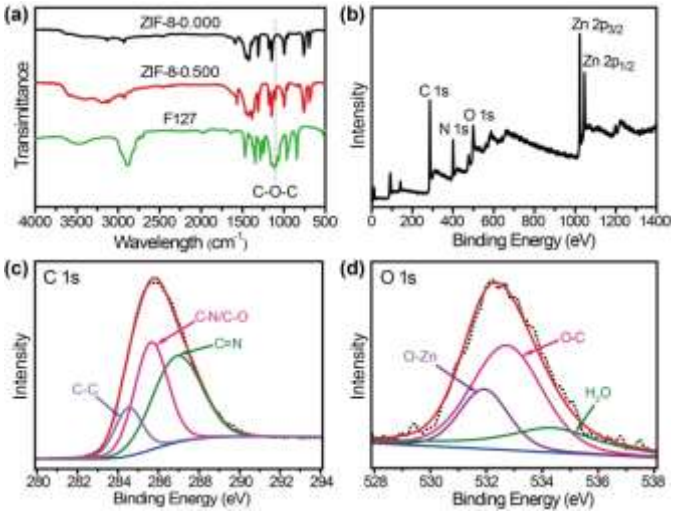

Figure 2. (a) FTIR spectra of F127 and representative ZIF-8 nanocrystals. (b) Wide-scan XPS spectra of ZIF-8-0.500 nanoribbons. (c and d) Deconvolutions of the C 1s and O 1s peaks shown in (b).

X-ray powder diffraction (XRD) patterns of the ZIF-8 nanocrystals are shown in Figure 1g. All samples exhibit diffraction patterns that can be easily indexed in accord with simulated spectrum[37], suggesting single phase of the products with a high crystallinity. The as-synthesized nanocrystals were also studied by thermogravimetry (TGA). As depicted in Figure 1h, all samples exhibit a weight loss in the temperature range from 450 to 740 °C, corresponding to the collapse of the frameworks of ZIF-8. For samples prepared in the presence of F127, an additional weight loss in 250–430 °C range was detected and ascribed to the decomposition of Pluronic F127. Notably, larger nanoribbons exhibit a higher percentage of weight loss from ZIF-8-0.000 to ZIF-8-0.500, implying that F127 molecules are primarily embedded in the interior of the nanoribbons. For ZIF-8-1.000, we detected a higher thermal stability and smaller weight loss, which is ascribed to reduced encapsulation of F127 associated with the nanoparticle morphology.

The size and crystallinity of a representative sample (ZIF-8-0.500) were then examined by atomic force microscopy (AFM) and transmission electron microscopy (TEM). The AFM image in Figure 1i shows thin thickness of the nanoribbons at the nanometer length scale (~33 nm). The TEM image along with the corresponding electron diffraction pattern (Figure 1j) reveal monocrystalline nature of the nanoribbons and preferential growth direction along the [001] axis.

The composition of the ZIF-8-0.500 nanoribbons was further characterized by Fourier transform infrared spectroscopy (FTIR) and X-ray photoelectron spectroscopy (XPS). The FTIR spectrum in Figure 2a shows absorption peaks at 1350-1500 cm^{-1} and 900-1350 cm^{-1} for ZIF-8-0.000 and ZIF-8-0.5000, which are associated with the stretching and in-plane bending of imidazole ring, respectively. The absorption peak at 1112 cm^{-1} observed from ZIF-8-0.500 nanoribbons was assigned to the C-O-C stretching of F127[39]. The results prove F127 was

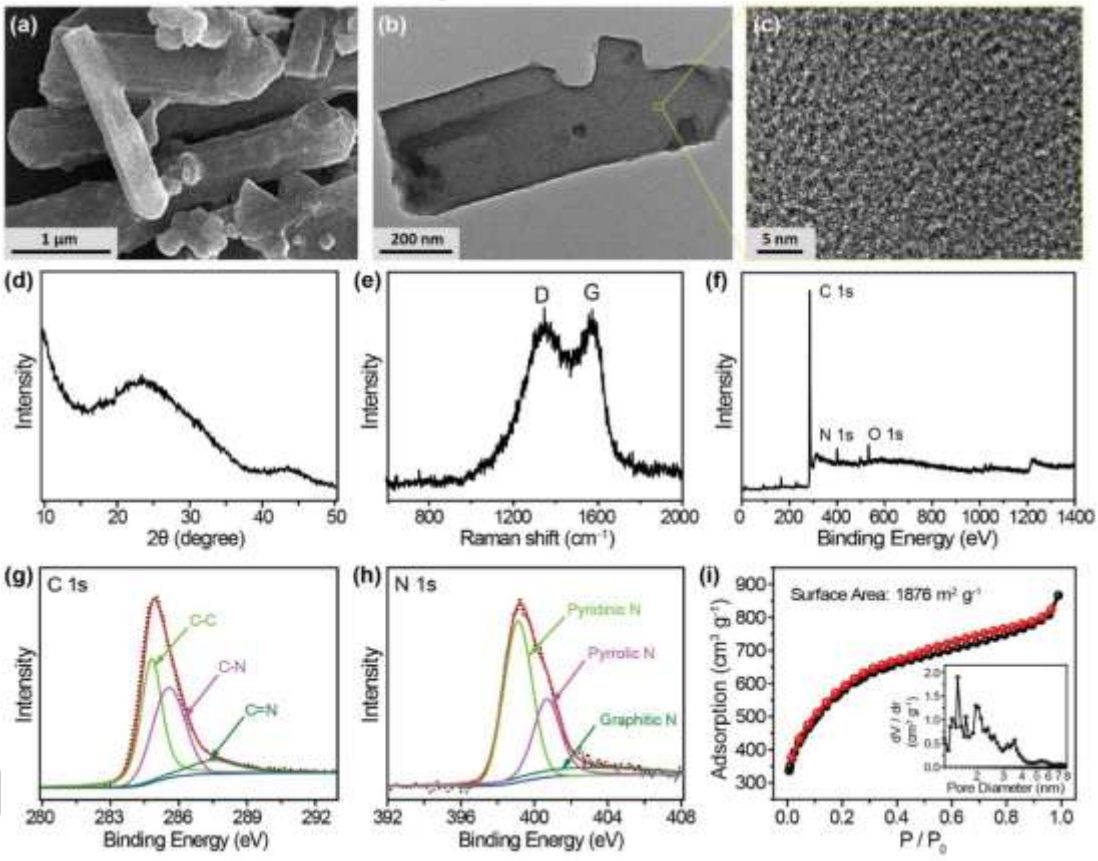

Figure 3. (a-c) SEM and TEM images, (d) XRD pattern, (e) Raman spectrum, and (f) XPS spectrum of the carbon nanoribbons derived from ZIF-8-0.500. (g and h) Deconvolutions of the C 1s and N 1s peaks shown in (f). (i) N_2 absorption (black curve) and desorption (red curve) isotherms of carbon nanoribbons derived from ZIF-8-0.500 at 77 K after activation with KOH. Inset: the pore-size distribution in the carbon nanoribbons.

presented in ZIF-8-0.5000. In order to probe the interior composition, the nanoribbons were stripped by 10 nm through ion etching. XPS spectrum of the stripped sample in Figure 2b shows principal C 1s, N 1s, O 1s, and Zn 2p peaks[40]. The C 1s peak can be resolved into three components centered at 284.5, 285.3 eV and 286.5, (Figure 2c), which are attributed to C-C, C-N/C-O, and C=N bonds, respectively[40-43]. For the O 1s peak (Figure 2d), three components centered at 532.0 eV, 533.2 eV, and 535.0 eV are resolved, corresponding to O-Zn, O-C, and residual H_2O, respectively[44].The results support incorporation of F127 molecules into interior of the ZIF-8 nanoribbons.

We next converted the ZIF-8 nanoribbons into carbon nanoribbons by calcination at 1000 °C, which was previously optimized for carbonization[45]. In order to maximize the porosity, the carbon nanoribbons were further activated by etching with KOH followed by annealing at 800 to eliminate the byproduct of K_2CO_3[46, 47]. SEM characterizations show that the size and morphology of the thermally-transformed samples are partially preserved (Figure 3a and Figure S2). The TEM image reveals noticeable breakage of the nanoribbons (Figure 3b), which is ascribed to the interaction with KOH and long-time ultrasonication. The high resolution TEM image in Figure 3c shows a disordered matrix of the nanoribbons, which is in agreement with XRD measurement showing two large bumps (Figure 3d). Raman scattering measurement detected both a disorder-induced D band (~1325 cm^{-1}) and a graphite-related G band (~1590 cm^{-1}) (Figure 3e), suggesting a distorted graphitic structure of the sample. The intensity ratio of the D band and the G band for the carbon nanoribbons derived from ZIF-8-0.500 is 0.98, which is close to graphene nanomaterials (1.0-1.5) synthesized by oxidative method[48]. Compositional analysis of the carbon nanoribbons by XPS reveals the presence of elemental N (Figure 3f), which is verified by electron energy loss spectroscopy (EELS) (Figure S3). By using the peak-fitting method, the concentration of C and N were estimated to be 94.51 wt% and 5.49 wt%, respectively. In addition, deconvolutions of the C 1s and N 1s peaks indicate the formation of C−N and C=N bonds (Figure 3g and h)[49,50], indicating the incorporation of N into the carbon structure.

The specific surface area and pore size distribution of the carbon nanoribbons were then studied by N_2 physisorption. Prior to KOH activation, mesopores were detected from carbon nanoribbons derived from ZIF-8-0.5000, but not from that derived from ZIF-8-0.000 (Figure S4). The observations validate the role of F127 in porous texture development of the carbon materials. After activation, appreciable increases in specific surface area and porosity were noted (Figure 3i and Figure S5), which is consistent with the study of Wang and Kaskel[47]. Furthermore, a high F127 content in the synthesis was found to promote the formation of mesopores (> 2nm) (Figure S5). Therefore, the pore structures in these carbon nanoribbons should be developed by decomposition of F127 under the thermal conditions and etching by KOH[51]. By using the Brunauer−Emmett−Teller (BET) method, a high specific surface area of 1876 m^2 g^{-1} were determined for the carbon nanoribbons derived from ZIF-8-0.500 (Figure 3i), which is comparable to typical porous carbon nanomaterials derived from ZIF-8 (784 m^2 g^{-1})[52].

To assess electrochemical properties of carbon nanoribbons, a three-electrode system was constructed using 3.0 M NaOH as the electrolyte. Cyclic voltammetry (CV) measurements on the carbon nanoribbons show voltammograms that generally derivate from rectangles (Figure 4a and Figure S6). The results are partially ascribed to the nitrogen dopants that undergo redox reactions due to a relatively high electronegativity[53].Further Galvanostatic charge/discharge (GCD) tests record triangular profiles and confirm excellent electrochemical capacitive properties (Figure 4b and Figure S7). Based on the GCD curves, the specific capacitance for the carbon nanoribbons derived from ZIF-8-0.500 was determined to be 297 F g^{-1} at a current density of 0.5 A g^{-1} (Figure 4c). The capacitance is largely preserved when the current density is increased from 0.5 to 8 A g^{-1}. For comparison, carbon nanomaterials derived from ZIF-8 nanocrystals synthesized with decreasing amount of F127 were also analyzed, which reveal steadily declining specific capacitances (Figure S8a). The reduction in capacitance is ascribed to decreased mesoporosity and length of the nanoribbons, which lead to slow ion and electron transport[54-56]. As confirmed by electrochemical impedance spectroscopy (EIS) measurements (Figure S9), deterioration of conductivity transport is clearly visible as the F127 content used for the synthesis of ZIF-8 precursors decreases. Notably, the specific capacitance achieved for the carbon nanoribbons is higher than most of existing carbon materials including commercial carbon black (18.9 F g^{-1}) and carbon nanotubes (30.2 F g^{-1}) (Figure S8b and Table S1). In addition, the carbon nanoribbons also show great stability. A 90.26% retention of the capacitance was recorded after 10, 000 cycles of charge-discharge at a current density of 4.0 A g^{-1} (Figure 4d).

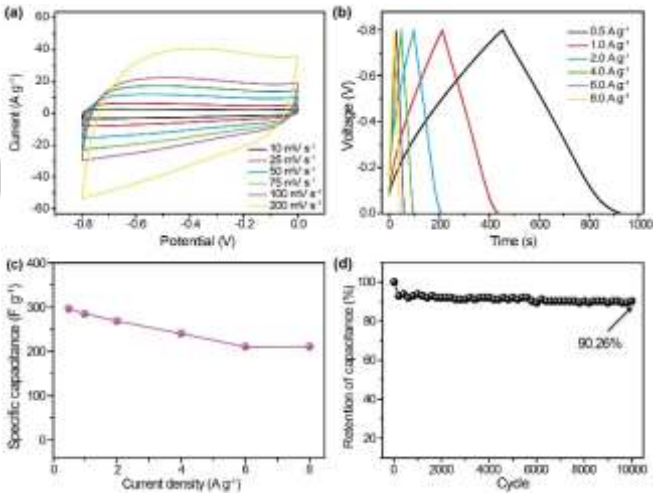

Figure 4. Assessment of electrochemical performances on a three-electrode system involving carbon nanoribbons derived from ZIF-8-0.500 as an electrode. (a) CV curves at different scan rates. (b) GCD curves at different current densities. (c) Specific capacitance calculated from the GCD curves in (b). (d) Cyclic stability at a current density of 4.0 A g^{-1}.

In a further set of experiments, we assessed the electrochemical performance on a two-electrode system, which is commonly used in practical settings. We assembled a two-electrode symmetrical supercapacitor using the carbon nanoribbons derived from ZIF-8-0.500 as electrode along with 3 M NaOH as electrolyte. Figure 5a shows the CV curves recorded in the potential window from 0 to 1.0 V at different scan rates from 0.1 A g^{-1} to 4.0 A g^{-1}. The shape of the CV curves

slightly deviates from the ideal rectangular shape and is ascribed to pseudo-capacitance associated with the N-doping. The GCD curves in Figure 5b exhibit the typical linear discharge curves, implying well-balanced charge storage of the symmetrical device[58]. The specific capacitance was as high as 132 F g^{-1} at the current density of 0.1 A g^{-1}, and preserved at 104 F g^{-1} when the current density increased to 4 A g^{-1} (Figure 5c). Correspondingly, a Ragone plot is compiled (Figure 5d and Table S2) and reveals an energy density of 18.4 Wh kg^{-1} at a power density of 100 W kg^{-1}. The energy density remained at 14.5 Wh kg^{-1} as the power density increased to 4000 W kg^{-1}, demonstrating a better performance of the symmetrical system than typical carbon nanomaterials-based supercapacitors[57-61]. Furthermore, the two-electrode symmetrical supercapacitor retained 84.40 % capacitance after 5000 cycles of operation at a current density of 2 A g^{-1} (Figure 5e). The Nyquist plot in Figure 5f shows small interfacial charge transfer resistance (Rct, ~3 Ω) and typical supercapacitive behavior. To demonstrate the scalable possibility, we further increased the mass loading of carbon nanoribbons to 10 mg cm^{-2}, which displayed a similar electrochemical performance (Figure S10). These results together indicate that the ZIF-8-derived carbon nanoribbons are promising electrode materials for supercapacitors.

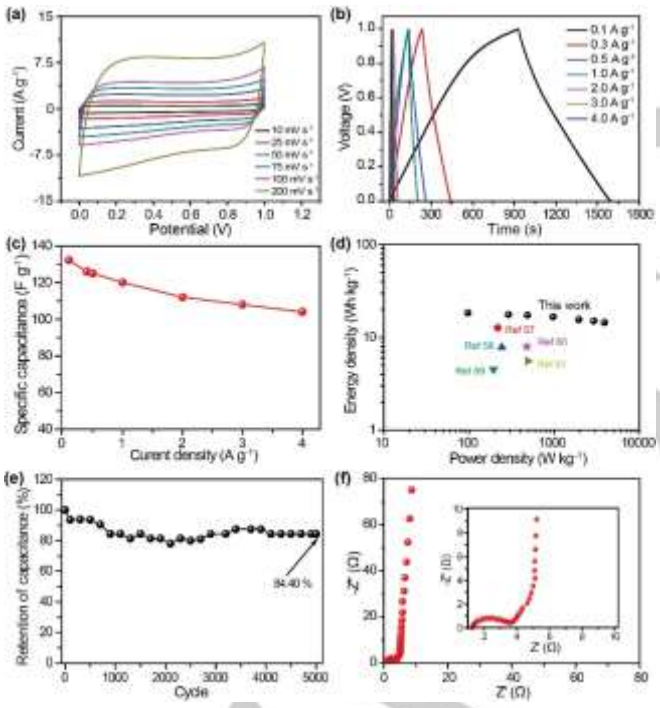

Figure 5. Assessment of electrochemical performances on a symmetrical two-electrode supercapacitor involving carbon nanoribbons derived from ZIF-8-0.500 as an electrode. (a) CV curves at different scan rates. (b) GCD curves at different current densities. (c) Specific capacitance calculated from the GCD curves in (b). (d) Ragone plot under various current densities. Typical literature data are also included for comparison. (e) Cyclic stability at a current density of 2.0 A g^{-1}. (f) Nyquist plots showing the imaginary part versus the real part of the impedance. Inset: impedance data in the high-frequency range.

Conclusions

In summary, we report a novel strategy of tuning carbon nanoribbons to cater for advanced energy applications. We show that carbon nanoribbons comprising both micro- and mesopores can be constructed by thermal transformation of ZIF-8 nanoribbons synthesized via a F127 mediated self-assembly process. F127 directs the formation of one-dimensional morphology and creates mesopores in the ZIF-8 nanocrystals. Owing to the unique porous structure derived from parent ZIF-8 nanoribbons, these carbon nanoribbons exhibit superb electrochemical performances including high specific capacitance (up to 297 F g^{-1}) and high cyclic stability. We expect further improvement of the electrochemical performance by reducing breakage of nanoribbons through refinement of the thermal transformation procedure.

Experimental Section

Materials

Zinc nitrate hexahydrate ($Zn(NO_3)_2{\cdot}6H_2O$), 2-methylimidazole (Hmim), F127, potassium hydroxide(KOH) and hydrochloric acid (HCl) were ordered from Sigma Aldrich. All chemicals were used as received without further purification.

Synthesis of ZIF-8 nanomaterials

ZIF-8 nanoribbons were synthesized through an evaporation induced self-assembly[62]. Typically, 0.15 g of zinc nitrate hexahydrate was added to a water solution of F127 (0 wt%, 0.125 wt%, 0.175 wt% 0.250 wt% , 0.500 wt%, or 1.000 wt%) and stirred for 30 minutes. Then, 1.65 g of Hmim was added and the mixture was stirred for another 30 minutes. The solution was then stood in a 30°C water bath overnight before being transferred to a petri dish and put into an oven at 80 °C for 24 h, during which time water was evaporated accompanying the formation of ZIF-8 nanoribbons. The products were washed with ethanol for several times and finally collected by centrifugation. The prepared samples are denoted as ZIF-8-0.000, ZIF-8-0.125, ZIF-8-0.175, ZIF-8-0.250, ZIF-8-0.500, and ZIF-8-1.000 according to the concentration of F127.

Preparation of carbon nanoribbons from ZIF-8

The method for preparation of carbon nanoribbons was adapted from report[19]. The as-synthesized ZIF-8 nanoribbons (e.g.; ZIF-8-0.500) seating in a ceramic boat were placed in a tube furnace under nitrogen flow. The sample was heated to 1000 °C at a heating rate of 1 °C min^{-1} and kept at this temperature for 4 h. The resultant black carbon nanoribbons were collected after being cooled to room temperature naturally. The carbon nanoribbons (0.1g) were then mixed with KOH (0.2 g) in distilled water (3 mL) and ultrasonicated for 30 min. The mixture was dried at 110 °C for 6 h to get the nanoribbons/KOH composite, which was then placed in a tube furnace and heated for 2 h under nitrogen atmosphere at 800 °C with a heating rate of 2 °C min^{-1}. The obtained products were washed with 1 M HCl and distilled water several times. The final product was collected by drying at 150 °C for 12 h. Following the same procedure, ZIF-8 nanocrystals prepared with different amounts of F127 were all converted to carbon nanocrystals for using as reference samples.

Characterization

Powder X-ray diffraction patterns were recorded on a D2 PHASER (BRUKER) diffractometer with Cu Kα irradiation. Thermo-gravimetric analysis was performed on Q1000 under nitrogen atmosphere from room temperature to 800 °C. The morphology was investigated by scanning electron microscopy (SEM, XL30, PHILIPS) at an acceleration voltage of 15 kV and transmission electron microscopy (TEM, Tecnai 12, PHILIPS)

at an acceleration voltage of 200 kV. The thickness of nanoribbons were measured by atomic force microscopy (AFM, Veeco di Multimode V). Fourier transform infrared (FTIR) spectroscopy spectra were obtained on a PerkinElmer Spectrum 100 using a KBr disk in the range of 4000 to 500 cm^{-1}. X-ray photoelectron spectroscopy (XPS) was carried on an ESCALAB 220i-XL electron spectrometer from VG Scientific using Al Kα irradiation. Raman spectrum was conducted on a Renishaw Raman spectrometer with a 514 nm laser as the excitation source. Nitrogen physisorption isotherms were measured at 77 K on a Quantachrome Nova 1200e Surface Area Analyser.

Electrochemical measurements

The electrochemical performance was tested on an electrochemical workstation (CHI760E, Shanghai Chen Hua Company) using 3 M NaOH as electrolyte. All the composite electrode was dried in a vacuum at 80 °C overnight and subsequently pressed under 3 MPa pressure to firmly fix the composite on the nickel foam. A three-electrode system that comprises a Pt wire as the counter electrode and a Ag/AgCl electrode as the reference electrode was constructed to evaluate the electrochemical performance of the obtained anode materials[63]. For the symmetrical supercapacitor, the positive and negative electrodes were prepared by the activated carbon nanoribbons derived from ZIF-0.500 and separated with each other by a distance of ~1 cm without any separator. The working electrode was prepared by loading slurry containing carbon nanoribbons (90 wt%) and polyvinylidene fluoride (PVDF, 10 wt.%) on a nickel foam with the mass loading content of 1.0 or 10 mg cm^{-2}.

Cyclic Voltammetry (CV) and Galvanostatic Charge/Discharge (GCD) curves were obtained within a fixed potential window of -0.8 to 0 for the three-electrode system and 0 to 1.0 V for the symmetrical two-electrode device at various scan rates and current densities. The Electrochemical Impedance Spectra (EIS) measurements were recorded under AC voltage amplitude of 5 mV in the frequency range from 10^5 Hz to 0.01 Hz. The cyclic stability of the as-prepared anode materials was measured by a battery measuring system (Lanhe, CT2001A) using the same electrode structures.

The specific capacitance (Cs), energy density (E), and power density (P) were calculated from the GCD curves through the equations (1)-(3)[57], respectively.

$$Cs=(I \times \Delta t)/(m \times \Delta V) \quad (1)$$

$$E=(1/2\ Cs\ \Delta V\text{^}2)/3.6 \quad (2)$$

$$P=3600 \times E/\Delta t \quad (3)$$

where Cs is the specific capacitance (F g^{-1}), I the current (A), ΔV the potential window, Δt the discharge time, and m the mass of activated materials (g).

Acknowledgements

This work was supported by City University of Hong Kong (SRG 7004650) and the Research Grants Council of Hong Kong (CityU 11306717). We thank X. Chen at Shenzhen University for help with sample characterizations.

Keywords: ZIF-8 nanoribbons • carbon nanoribbons • micropore •mesopore • supercapacitor

[1] J. Lee, J. Kim and T. Hyeon, *Adv. Mater.* **2006**, 18, 2073-2094.
[2] M. J. Allen, V. C. Tung and R. B. Kaner, *Chem. Rev.* **2010**, 110, 132-145.
[3] Z.-M. Dang, M.-S. Zheng and J.-W. Zha, *Small* **2016**, 12, 1688-1701.
[4] D. S. L. Abergel, V. Apalkov, J. Berashevich, K. Ziegler and T. Chakraborty, *Adv. Phys*. **2010**, 59, 261-482.
[5] Z. Zhang, C.-S. Lee and W. Zhang, *Adv. Energy. Mater.* DOI: 10.1002/aenm.201700678.
[6] S. B. Yoon, K. Sohn, J. Y. Kim, C. H. Shin, J. S. Yu and T. Hyeon, *Adv. Mater.* **2002**, 14, 19-21.
[7] P. Strubel, S. Thieme, T. Biemelt, A. Helmer, M. Oschatz, J. Brückner, H. Althues and S. Kaskel, *Adv. Funct. Mater.* **2015**, 25, 287-297.
[8] T. Kyotani, Z. Ma and A. Tomita, *Carbon* **2003**, 41, 1451-1459.
[9] X. Cao, C. Tan, M. Sindoro and H. Zhang, *Chem. Soc. Rev*. **2017**, DOI: 10.1039/c6cs00426a.
[10] W. Chaikittisilp, K. Ariga and Y. Yamauchi, *J. Mater. Chem. A* **2013**, 1, 14-19.
[11] C. Young, J. Wang, J. Kim, Y. Sugahara, J. Henzie and Y. Yamauchi, Chem. Mater., **2018**, DOI: 10.1021/acs.chemmater.8b00836.
[12] C. Wang, Y. V. Kaneti, Y. Bando, J. Lin, C. Liu, J. Li and Y. Yamauchi, Materials Horizons, **2018**, 5, 394-407.
[13] O. M. Yaghi, M. O'Keeffe, N. W. Ockwig, H. K. Chae, M. Eddaoudi and J. Kim, *Nature* **2003**, 423, 705-714.
[14] L. Wen-Hua, D. Kui, T. Han-Rui, Y. Ming-Shui, N. Bhaskar, D. Wei-Hua, W. Yaobing and X. Gang, *Adv. Funct. Mater*., **2017**, 27, 1702067.
[15] Y. Ming-Shui, L. Xiao-Jing, F. Zhi-Hua, L. Wen-Hua, D. Wei-Hua, W. Guo-Dong and X. Gang, *Angew. Chem. Int. Ed*., **2017**, 56, 16510-16514.
[16] R. R. Salunkhe, Y. V. Kaneti, J. Kim, J. H. Kim and Y. Yamauchi, *Acc. Chem. Res.* **2016**, 49, 2796-2806.
[17] K. Shen, X. Chen, J. Chen and Y. Li, ACS Catalysis **2016**, 6, 5887-5903.
[18] J. Tang and Y. Yamauchi, *Nat Chem*, **2016**, 8, 638-639.
[19] P. Pachfule, D. Shinde, M. Majumder and Q. Xu, *Nat. Chem*. **2016**, 8, 718-724.
[20] Z.-Y. Gu, C.-X. Yang, N. Chang and X.-P. Yan, *Acc. Chem. Res*. **2012**, 45, 734–745.
[21] P. Zhang, B. Y. Guan, L. Yu and X. W. Lou, *Angew. Chem. Int. Ed*. **2017**, 56, 7141-7145.
[22] J. Cravillon, C. A. Schroder, H. Bux, A. Rothkirch, J. Caro and M. Wiebcke, *CrystEngComm*. **2012**, 14, 492-498.
[23] R. R. Salunkhe, Y. Kamachi, N. L. Torad, S. M. Hwang, Z. Sun, S. X. Dou, J. H. Kim and Y. Yamauchi, *J. Mater. Chem. A* **2014**, 2, 19848-19854.
[24] W. Chaikittisilp, M. Hu, H. Wang, H.-S. Huang, T. Fujita, K. C. W. Wu, L.-C. Chen, Y. Yamauchi and K. Ariga, *Chem. Commun*. **2012**, 48, 7259-7261.
[25] J. Tang, R. R. Salunkhe, J. Liu, N. L. Torad, M. Imura, S. Furukawa and Y. Yamauchi, *J. Am. Chem. Soc*. **2015**, 137, 1572-1580.
[26] C. Liu, X. Huang, J. Wang, H. Song, Y. Yang, Y. Liu, J. Li, L. Wang and C. Yu, *Adv. Funct. Mater*. **2017**, 28, 1705253.
[27] C. Wang, C. Liu, J. Li, X. Sun, J. Shen, W. Han and L. Wang, *Chem Commun. (Camb)* **2017**, 53, 1751-1754.
[28] K. S. Park, Z. Ni, A. P. Côté, J. Y. Choi, R. Huang, F. J. Uribe-Romo, H. K. Chae, M. O'Keeffe and O. M. Yaghi, *Proc. Natl. Acad. Sci.* **2006**, 103, 10186-10191.
[29] J. Zhang, L. Yu and X. W. D. Lou, *Nano Res.* **2017**, DOI: 10.1007/s12274-016-1394-1.
[30] J. Kim, C. Young, J. Lee, Y.-U. Heo, M.-S. Park, M. S. A. Hossain, Y. Yamauchi and J. H. Kim, *J. Mater. Chem. A* **2017**, 5, 15065-15072.
[31] J. Kim, C. Young, J. Lee, M.-S. Park, M. Shahabuddin, Y. Yamauchi and J. H. Kim, *Chem. Commun*. **2016**, 52, 13016-13019.
[32] C. Young, R. R. Salunkhe, J. Tang, C.-C. Hu, M. Shahabuddin, E. Yanmaz, M. S. A. Hossain, J. H. Kim and Y. Yamauchi, *PCCP* **2016**, 18, 29308-29315.
[33] Y. Pan, D. Heryadi, F. Zhou, L. Zhao, G. Lestari, H. Su and Z. Lai, *CrystEngComm*. **2011**, 13, 6937-6940.
[34] K. Kida, M. Okita, K. Fujita, S. Tanaka and Y. Miyake, *CrystEngComm*. **2013**, 15, 1794-1801.
[35] M. Karayianni and S. Pispas, Fluorescence Studies of Polymer Containing Systems, *Springer* **2016**, pp 27-63.
[36] C. Chaibundit, N. M. P. S. Ricardo, F. d. M. L. L. Costa, S. G. Yeates and C. Booth, *Langmuir*. **2007**, 23, 9229-9236.
[37] Y. Pan, Y. Liu, G. Zeng, L. Zhao and Z. Lai, *Chem. Commun*. **2011**, 47, 2071-2073.
[38] Z. Li, H. Yan, S. Yuan, Y. Fan and J. Zhan, J. *Colloid Interface Sci*. **2011**, 354, 89-93.
[39] Y.-L. Su, J. Wang and H.-Z. Liu, Macromolecules **2002**, 35, 6426-6431.
[40] J. Li, Y.-N. Wu, Z. Li, B. Zhang, M. Zhu, X. Hu, Y. Zhang and F. Li, *J. Phys. Chem. C* **2014**, 118, 27382-27387.
[41] G. P. López, D. G. Castner and B. D. Ratner, Surf. Interface Anal. **1991**, 17, 267-272.
[42] T. I. T. Okpalugo, P. Papakonstantinou, H. Murphy, J. McLaughlin and N. M. D. Brown, *Carbon* **2005**, 43, 153-161.
[43] X. Y. Chen, Y. Y. He, H. Song and Z. J. Zhang, *Carbon* **2014**, 72, 410-420.
[44] R. Li, X. Ren, X. Feng, X. Li, C. Hu and B. Wang, *Chem. Commun*. **2014**, 50, 6894-6897.
[45] Y. Liu, X. Xu, M. Wang, T. Lu, Z. Sun and L. Pan, *Chem. Commun*. **2015**, 51, 12020-12023.
[46] D. Lozano-Castelló, J. M. Calo, D. Cazorla-Amorós and A. Linares-Solano, *Carbon* **2007**, 45, 2529-2536.
[47] J. Wang and S. Kaskel, *J. Mater. Chem*. **2012**, 22, 23710-23725.

[48] L. Jiao, L. Zhang, X. Wang, G. Diankov and H. Dai, *Nature* **2009**, 458, 877-880.
[49] J. Shalini, K. J. Sankaran, C. L. Dong, C. Y. Lee, N. H. Tai and I. N. Lin, *Nanoscale* **2013**, 5, 1159-1167.
[50] F. Zheng, Y. Yang and Q. Chen, *Nat. Commun.* **2014**, 5, 5261-5270.
[51] J. Górka, A. Zawislak, J. Choma and M. Jaroniec, *Carbon* **2008**, 46, 1159-1161.
[52] R. Wang, D. Jin, Y. Zhang, S. Wang, J. Lang, X. Yan and L. Zhang, *J. Mater. Chem. A* **2017**, 5, 292-302.
[53] W. Qian, F. Sun, Y. Xu, L. Qiu, C. Liu, S. Wang and F. Yan, *Energy Environ. Sci.* **2014**, 7, 379-386.
[54] D. Zhang, X. Wen, L. Shi, T. Yan and J. Zhang, *Nanoscale* **2012,** 4, 5440-5446.
[55] Y. Kado, K. Imoto, Y. Soneda and N. Yoshizawa, *J. Power Sources* **2014**, 271, 377-381.
[56] W. Chen, R. B. Rakhi, L. Hu, X. Xie, Y. Cui and H. N. Alshareef, *Nano Lett.*, **2011**, 11, 5165-5172.
[57] X. Li, C. Hao, B. Tang, Y. Wang, M. Liu, Y. Wang, Y. Zhu, C. Lu and Z. Tang, *Nanoscale* **2017**, 9, 2178-2187.
[58] Y. Huang, L. Peng, Y. Liu, G. Zhao, J. Y. Chen and G. Yu, *ACS Appl. Mat. Interfaces* **2016**, 8, 15205-15215.
[59] F. Miao, C. Shao, X. Li, K. Wang, N. Lu and Y. Liu, *J. Mater. Chem. A* **2016**, 4, 5623-5631.
[60] F. Ma, D. Ma, G. Wu, W. Geng, J. Shao, S. Song, J. Wan and J. Qiu, *Chem. Commun*. **2016**, 52, 6673-6676.
[61] H. An, Y. Li, P. Long, Y. Gao, C. Qin, C. Cao, Y. Feng and W. Feng, *J. Power Sources* **2016**, 312, 146-155.
[62] L. Mahoney and R. Koodali, *Materials* **2014**, 7, 2697-2746.
[63] W. Meng, W. Chen, L. Zhao, Y. Huang, M. Zhu, Y. Huang, Y. Fu, F. Geng, J. Yu, X. Chen and C. Zhi, *Nano Energy* **2014**, 8, 133-140.

10.1002/chem.201801869

FULL PAPER

ZIF-8 nanoribbons with tunable morphology and pore structure were synthesized by using tri-block co-polymer Pluronic F127 as a soft template. The ZIF-8 nanoribbons were converted to porous carbon nanoribbons by morphology-preserved thermal transformation. The unique morphology was demonstrated to promote electrochemical performance of carbon nanomaterials.

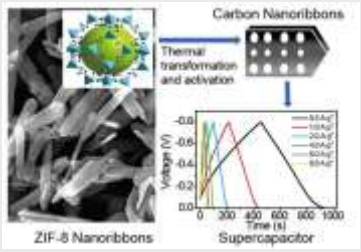

*Xueqing Yang, Wei Chen, Haidong Bian, Tianying Sun, Yangyang Du,Zhenyu Zhang, Wenjun Zhang, Yangyang Li, Xianfeng Chen, Feng Wang**

Page No.1 – Page No.8

Title

Synthesis of Mesoporous ZIF-8 Nanoribbons and Their Conversion into Carbon Nanoribbons for High-Performance Supercapacitors